# Elasticity of a Pseudoproper Ferroelastic Transition from Stishovite to Post-Stishovite at High Pressure

Yanyao Zhang, Suyu Fu, Baoyun Wang, and Jung-Fu Lin

Phys. Rev. Lett. **126**, 025701 — Published 12 January 2021

DOI: 10.1103/PhysRevLett.126.025701

# Elasticity of Pseudo-proper Ferroelastic Transition from Stishovite to Post-Stishovite at High Pressure

Yanyao Zhang,[1] Suyu Fu,[1] Baoyun Wang,[2] and Jung-Fu Lin[1,*]

[1] *Department of Geological Sciences, Jackson School of Geosciences, The University of Texas at Austin, Austin, Texas 78712, USA*

[2] *State Key Laboratory of Isotope Geochemistry, Guangzhou Institute of Geochemistry, Chinese Academy of Sciences, Guangzhou 510640, China*

*To whom correspondence should be addressed: afu@jsg.utexas.edu

## Abstract

Elastic moduli ($C_{ij}$'s) of single-crystal stishovite and post-stishovite are determined using Brillouin light scattering, impulsive stimulated light scattering, and X-ray diffraction up to 70 GPa. The $C_{12}$ of stishovite converges with the $C_{11}$ at ~55 GPa, where the transverse wave $V_{S1}$ propagating along [110] also vanishes. Landau modelling of the $C_{ij}$'s, $B_{1g}$ optic mode, and lattice parameters reveals a pseudo-proper type ferroelastic post-stishovite transition. The transition would cause peculiar anomalies in $V_S$ and Poisson's ratio in silica-bearing subducting slabs in the mid-lower mantle.

*Introduction*-Ferroelastic transitions are physical phenomena in which crystals undergo a change in point group ("a change of forms") with a symmetry-breaking shear strain [1,2]. Ferroelastic crystals are thus regarded as mechanical analogues of ferromagnetics and ferroelectrics, which are at the heart of novel multiferroic materials for condensed matter physics research and industrial applications [3,4]. Hydrostatic pressure generated in a diamond anvil cell (DAC) can serve as a more effective thermodynamic means than temperature to induce a very large spontaneous strain so the mechanism of the ferroelastic transition could be deciphered [5]. To better understand its underlying driving force, it is of paramount importance to investigate the full sets of elastic moduli ($C_{ij}$'s) across the transition [6,7]. Insofar, high-pressure experimental studies on ferroelastic transitions are often limited to optic modes by Raman and infrared spectroscopy as well as lattice parameters and equation of states (EoS) by X-ray diffraction (XRD) [8,9]. Reliable measurements on the full $C_{ij}$'s, however, remain limited due to technical challenges in measuring single-crystal sound velocities of both paraelastic and ferroelastic phases across the transition.

Ferroelastic transitions occur naturally in oxides and silicates in Earth's deep crust and mantle, and have been reported to cause seismic velocity anomalies [10,11]. The ferroelastic transition in stishovite ($SiO_2$) is of particular interest in geophysics due to its abundance of ~25 vol%  in basaltic subducting slabs [12]. Stishovite is a prototype of six-fold coordinated oxides and silicates, and is known to display a number of unusual physical properties: a high density of 4.28 g/cm$^3$, high adiabatic bulk modulus ($K_S$) of 308 GPa, and high shear modulus ($\mu$) of 228 GPa at ambient conditions [13,14]. Stishovite has also attracted significant interest in materials science as an analog for finding novel superhard and incompressible materials [15]. Previous studies have shown that rutile-type stishovite (space group: $P4_2/mnm$; point group: 422) transforms into $CaCl_2$-type post-stishovite (space group: *Pnnm*; point group: 222) at ~50-55 GPa and room temperature [16]. The tetragonal-to-orthorhombic transition is manifested by a softening of the $B_{1g}$ optic mode in stishovite [17]. In a pseudo-proper type Landau model, the order parameter for the transition is bilinearly coupled with a symmetry-breaking shear strain in post-stishovite [18] and the modelled elastic moduli show a significant shear softening across the transition [19-21]. Furthermore, first-principle calculations showed that the transition is driven by a strong coupling between elastic moduli and softening of the $B_{1g}$ mode [22,23]. Direct experimental measurements on single-crystal $V_P$ and $V_S$ velocities to derive full $C_{ij}$'s of stishovite and post-stishovite at high pressure would provide key information about the nature of the ferroelastic transition. However, reliable determinations of the full $C_{ij}$'s of stishovite are currently limited to ~12 GPa using the Brillouin light scattering (BLS) technique [14,24-26]. This limitation is mainly due to the relatively high $V_P$ of stishovite at ~12-13 km/s that would have overlapped with the $V_S$ of diamond anvils in DACs. Advent on high-pressure velocity measurements of stishovite is also needed to enhance our knowledge of the ferroelastic transition.

In this letter, we have used both Impulsive Stimulated Light Spectroscopy (ISLS) and BLS techniques to measure $V_P$ and $V_S$ of single-crystal stishovite and $CaCl_2$-type post-stishovite up to 70 GPa at room temperature. Together with complementary XRD results, we have solved their full $C_{ij}$'s and analyzed acoustic wave dispersions along critical points of the first Brillouin zone across the post-stishovite transition. Based on the pseudo-proper type Landau modelling, our results reveal that the transition is driven by the soft $B_{1g}$ mode. The coupling between the order parameter and the symmetry-breaking spontaneous strain is manifested by ($C_{11}$-$C_{12}$) approaching zero and a disappearance of $V_{S1[110]}$ propagating along [110] and polarized along $[1\bar{1}0]$. These results of the post-stishovite transition are also used to provide new insights into other ferroelastic transitions as well as abnormal seismic wave signatures in subducting slabs in the lower mantle.

*Results*-The collected BLS and ISLS spectra up to 70 GPa display high signal-to-noise ratios and are used to derive $V_P$ and $V_S$ of single-crystal stishovite and post-stishovite at high pressure (Figs. 1 and S1-S5; Tables SI and SII; Text S1 and S2 in [27]) [28-34]. Two transverse acoustic velocities with mutually orthogonal polarizations, $V_{S1}$ and $V_{S2}$, are observed in BLS spectra of both phases, where $V_{S2}$ is larger than $V_{S1}$ by definition. Together with the EoS from XRD results (Figs. S6 and S7; Tables SIII and SIV) [27,35-37], the $V_{S1}$, $V_{S2}$, and $V_P$ values as a function of azimuthal angles are used to solve for full $C_{ij}$'s of stishovite and post-stishovite at each experimental pressure using Christoffel's equations [38]. Uncertainties of all elastic constants except $C_{11}$ of the post-stishovite phase are sufficiently small for examinations of their pressure-dependent trends across the transition [39] (Text S3 in [27]). Our derived $C_{ij}$'s of stishovite at pressures below 12 GPa are consistent with a previous BLS study (Fig. 2) [14].

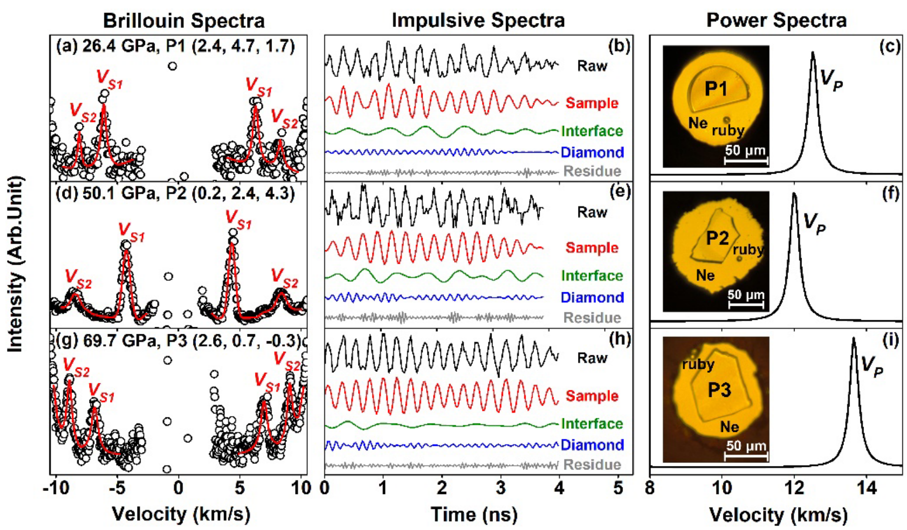


FIG. 1. Representative BLS and ISLS spectra of single-crystal stishovite and post-stishovite at high pressure. Pressures and crystallographic orientations of each platelet are labeled in BLS panels. Open circles in (a), (d), and (g) are collected raw BLS data while red lines are best fits to derive $V_{S1}$ and $V_{S2}$ of the crystal. ISLS spectra in (b), (e), and (h) display signals of the sample, interface, and diamond extracted from the raw data. (c), (f), and (i) are modelled power spectra for the derived $V_P$ of the sample. Inserts show representative optical images of the sample chambers.

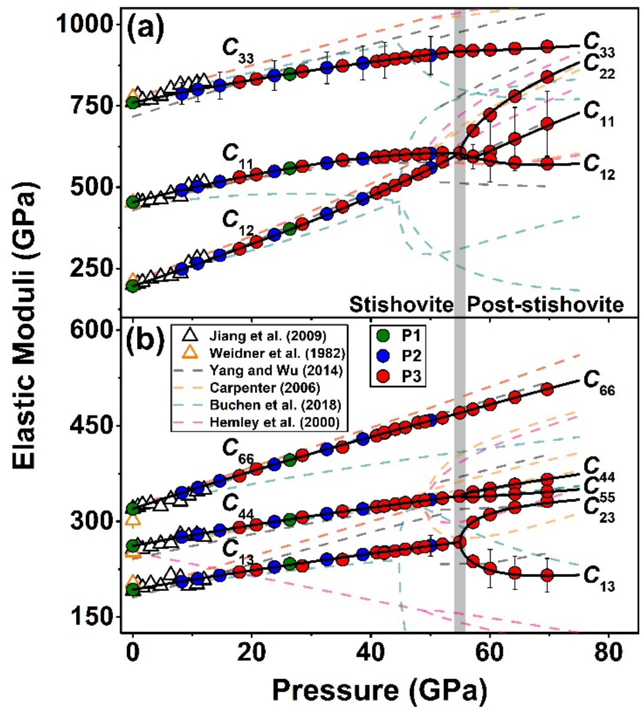


FIG. 2. Elastic moduli of single-crystal stishovite and post-stishovite at high pressure. Solid circles are derived $C_{ij}$'s values in this study and solid black lines represent best fits using Landau theory modelling [20,40]. Error bars are smaller than symbols when not shown. The grey vertical band represents the ferroelastic transition region at ~55 GPa. Literature data are also plotted for comparison [14,19,23,24,41,42].

The derived $C_{ij}$'s of stishovite show that all but $C_{11}$ and $C_{12}$ moduli increase almost linearly with increasing pressure up to 55 GPa (Fig. 2). The three moduli sets of stishovite, principle longitudinal moduli ($C_{11}$ and $C_{33}$), shear moduli ($C_{44}$ and $C_{66}$), and off-diagonal moduli ($C_{12}$ and $C_{13}$), gradually diverge from each other at high pressure. These indicate that the stishovite lattice is experiencing enhanced anisotropic compressional and shear strains with increasing pressure. Most importantly, the $C_{12}$ modulus, which relates a compressional stress (σ) to a perpendicular compressional strain (ε), increases significantly with pressure, while the $C_{11}$ modulus flattens above ~40 GPa. These lead to the convergence of $C_{11}$ and $C_{12}$ at ~55 GPa. That is, the ($C_{11}$ – $C_{12}$)/2 constant, which reflects the response of a crystal to deformation caused by shear stress along the [110] direction [43], vanishes at the transition [Fig. 3(a)]. This, in turn, is responsible for the second-order lattice distortion transition where the tetragonal *a* axes of the stishovite phase split into the orthorhombic *a* and *b* axes in the post-stishovite phase [Figs. 3(b) and S7(a)]. Such shear-induced lattice distortion also results in rotation of $SiO_6$ octahedra within the *a* axes plane, causing softening of the $B_{1g}$ optic mode [Figs. 4(a) and S8; Table SV].

Crossing into the orthorhombic post-stishovite, three new elastic moduli $C_{22}$, $C_{55}$, and $C_{23}$ emerge and deviate from $C_{11}$, $C_{44}$, and $C_{13}$, respectively, with increasing pressure (Fig. 2). The three principle longitudinal moduli follow the trend $C_{33} > C_{22} > C_{11}$ which indicates anisotropic lattice distortion: the two polar Si-O bonds in the *a*-*b* plane are more compressible than the four equatorial Si-O bonds in the planes parallel to the *c* axis in $SiO_6$ octahedra, consistent with XRD refinement results [16]. On the other hand, off-diagonal $C_{12}$ and $C_{13}$ moduli, which relate to shear distortion in the [110] and [101] directions, respectively, soften with increasing pressure [Fig. 3(b)]. This leads to an enhanced transverse wave velocity in these directions, and thus, stabilizes the orthorhombic post-stishovite phase [Fig 3(d)].

The elastic moduli results are further used to analyze $V_P$ and $V_S$ dispersions along the principal crystallographic axes ([100], [010], and [001]) and diagonal directions of the principle lattice planes ([101], [011], and [110]) across the post-stishovite transition [Figs. 3(c), (d), and 4(b)]. Results show that $V_{S1[110]}$ propagating along [110] and polarizing along [1$\bar{1}$0] vanishes at ~55 GPa, while all other acoustic waves vary minimally across the transition.

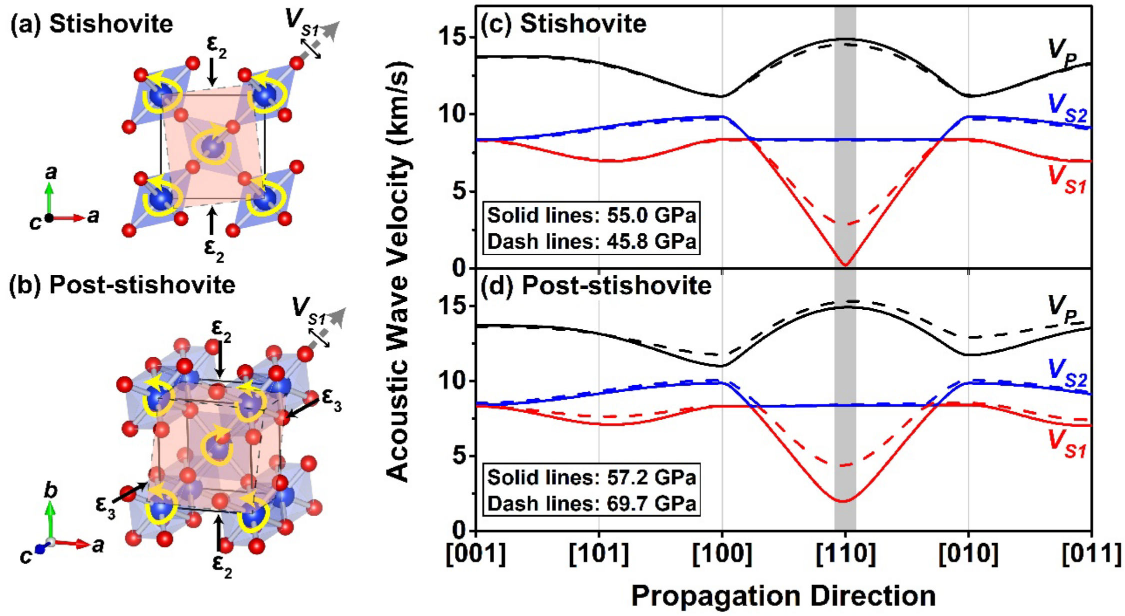


FIG. 3. Lattice distortions and acoustic wave velocity dispersions across the post-stishovite transition at high pressure. (a) and (b) depict the lattice shear distortion across the ferroelastic transition. Blue and red spheres denote Si and O atoms, respectively. The tetragonal (a) and orthorhombic (b) unit cells under strains are schematically shown in red areas with dashed lines. The strains, labelled as $\varepsilon_2$ and $\varepsilon_3$, depict that the off-diagonal moduli, $C_{12}$ and $C_{13}$, become anomalous (see Fig. 2). (c) and (d) show velocity dispersions of $V_P$ (black lines), $V_{S2}$ (blue lines), and $V_{S1}$ (red lines) across the transition. The $V_{S1}$ disappears at the transition that propagates along [110] [dashed gray lines with arrows in (a) and (b)] and has polarization along [1$\bar{1}$0] (thin black lines with arrows).

*Discussion and Implications*- In order to better understand the transformation mechanism, our experimental $C_{ij}$'s results as well as Raman and X-ray diffraction data are modelled using the Landau theory with a pseudo-proper type energy expansion where the soft $B_{1g}$ mode would lead to the phase transition (Figs. 2, 4, S9, and S10; Table SVI; Text S4 and S5 in [27]). This Landau model assumes that the order parameter (Q) is coupled bilinearly with the symmetry-breaking spontaneous strain, $(e_1-e_2)/\sqrt{2}$ (Eqs. S13 to S15) and the coupling would lead to a nonlinear decrease of the $(C_{11}-C_{12})$ approaching zero at the transition. The Landau modelling results are very consistent with our experimental elastic moduli across the transition (Fig. 2).

We have also examined the elastic stability across the post-stishovite transition using Born stability criteria [Fig. 4(c)] [44]. Born criteria reflecting the shear stability and the bulk modulus of stishovite are $B_1^{St} = C_{11} - C_{12} > 0$ and $B_2^{St} = C_{33}(C_{11} + C_{12}) - 2C_{13}^2 > 0$, respectively. The ($C_{11}$-$C_{12}$) value in the $B_1^{St}$ criterion is an eigenvalue to a strain eigenvector with the $B_{1g}$ symmetry and the $(e_1\text{-}e_2)/\sqrt{2}$ spontaneous strain based on the group theory [21]. Based on the Landau theory, the consequence of the coupling between the order parameter and the spontaneous strain is that the ($C_{11}$-$C_{12}$) value becomes zero at the transition. The $B_2^{St}$, relating to bulk modulus, remains positive and monotonously increases with pressure. That is, the unit cell volume is subjected to a continuous bulk compression without exhibiting a discontinuous volume collapse in the second-order lattice distortion transition. Furthermore, two Born criteria for the shear stability of the orthorhombic post-stishovite are $B_1^{Pst} = C_{11}C_{22} - C_{12}^2 > 0$ and $B_2^{Pst} = C_{11}C_{22}C_{33} + 2C_{12}C_{13}C_{23} - C_{11}C_{23}^2 - C_{22}C_{13}^2 - C_{33}C_{12}^2 > 0$. These values also become zero at the transition. Finally, the transverse acoustic wave $V_{S1[110]}$ and the two Born stability criteria, $B_1^{Pst}$ and $B_2^{Pst}$, reemerge at pressures above the transition. The $A_g$ mode in post-stishovite, which has similar vibrational rotations to those of the $B_{1g}$ mode, is also stiffened with increasing pressure.

Putting all the pieces together, our results provide a comprehensive picture for the stishovite to post-stishovite ferroelastic transition. Stishovite undergoes an anisotropic compression under high pressure, which leads to a shear-driven lattice distortion and the softening of the $B_{1g}$ optic mode. The reduction of symmetry, a change of forms from the tetragonal point group to the orthorhombic point group, across the transition induces the symmetry-breaking spontaneous strain in the low-symmetry post-stishovite phase. The soft mode would become imaginary at the critical pressure ($P_C$ = ~110.2 GPa). However, the transition actually occurs at $P_C^*$ = ~55 GPa, much lower than the $P_C$, due to a bilinear coupling between the order parameter and the symmetry-breaking $(e_1\text{-}e_2)/\sqrt{2}$ spontaneous strain [Fig. 4(a) and (d)]. This coupling further results in the eigenvalue $B_1^{St}$ ($C_{11}$-$C_{12}$) and acoustic wave $V_{S1[110]}$ nonlinearly decreasing to zero with increasing pressure up to $P_C^*$. Therefore, the post-stishovite transition is clearly driven by the soft $B_{1g}$ mode and belongs to the pseudo-proper Landau-type phase transformation [21].

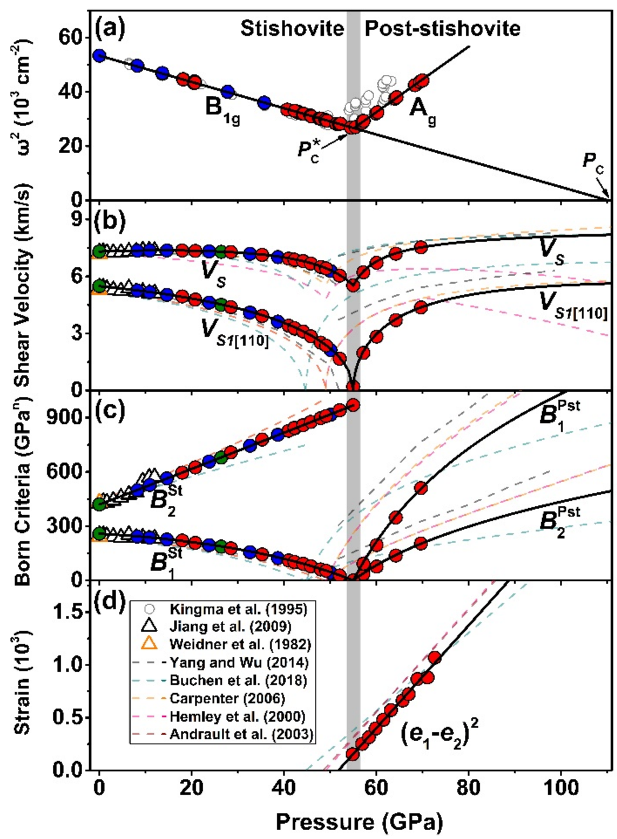


FIG. 4. Optical, elastic, and mechanical behaviors across the post-stishovite transition. (a) Pressure dependence of squared Raman shifts ($\omega^2$) of $B_{1g}$ and $A_g$ mode, where the transition pressure ($P_C^*$) and critical pressure ($P_C$) are labelled. (b) $V_{S1[110]}$ vanishes and aggregate $V_S$ softens at the transition. (c) Born stability criteria $B_1^{St}$ (in GPa), $B_1^{Pst}$ (in $5\times10^2$ GPa$^2$), and $B_2^{Pst}$ (in $10^6$ GPa$^3$) vanish at the transition whereas $B_2^{St}$ (in $10^3$ GPa$^2$) does not. (d) Squared symmetry-breaking spontaneous strain $(e_1\text{-}e_2)^2$ emerges in the post-stishovite phase. Experimental data from this study are plotted as solid circles. Black solid lines are results from the Landau model. Early studies are also shown for comparison [14,17-19,23,24,41,42]. The grey vertical band shows the transition pressure.

The nature of the post-stishovite transition could be used to understand other ferroelastic systems such as the tetragonal-monoclinic transition in $BiVO_4$ at 1.5 GPa [45]. The optic $B_g$ mode in tetragonal $BiVO_4$ softens close to the transition while the $A_g$ mode in the monoclinic structure stiffens after the transition [46]. The transverse wave $V_{S1}$ in the (001) plane vanishes at the transition in both phases [47]. Our results can thus help elucidate the nature of the ferroelastic transition in other systems.

Our results also have implications on deep-mantle geophysics, where the post-stishovite transition likely occurs at ~1800 km (or 77 GPa and 1706 K) in cold subducting slabs [48]. Using our elasticity data and theoretical predictions to evaluate the high pressure-temperature effect on elasticity [23], the post-stishovite transition would have a minimum aggregate $V_S$ of 5.52 km/s and a Poisson's ratio of 0.363 at ~1800 km depth [49]. Considering a subducting slab containing mid-ocean ridge basalt with ~25 vol% of stishovite [12], the post-stishovite transition would result in approximately 5.4% reduction in $V_S$ and 5.5% enhancement in Poisson's ratio (Text S6 in [27]) [50,51]. The effects of the ferroelastic transition on the aforementioned seismic parameters are expected to be distinct from structural transitions and temperature-compositional perturbations more commonly found in the mantle. Seismic observations on the mantle with reduced $V_S$ and enhanced Poisson's ratio near subducting slabs can thus be used as telltale signs [10] to relate to the naturally occurring ferroelastic transition.

*Conclusion*-The experimentally-derived full $C_{ij}$'s, Raman, and X-ray diffraction data of single-crystal stishovite and post-stishovite reveal the nature of the ferroelastic transition at ~55 GPa. Under quasi-hydrostatic pressure, enhancement of the anisotropic compression leads to the tetragonal-orthorhombic lattice distortion, which is manifested in softening of the $B_{1g}$ optic mode. Due to the coupling of the order parameter with the spontaneous strains, the ferroelastic transition occurs at 55 GPa where the $C_{11}$ modulus converges with the $C_{12}$ modulus and $V_{S1[110]}$ vanishes. As the distortion continues into the orthorhombic post-stishovite phase, large spontaneous strains occur while $V_{S1[110]}$ recovers in the ferroelastic phase. The post-stishovite transition can be well explained by the pseudo-proper type energy expansion within the framework of Landau theory. The transition is expected to occur in subducting slabs containing basalt at ~1800 km depth with seismic signatures of ~5.4% $V_S$ reduction and ~5.5% Poisson's ratio enhancement in the lower mantle.

## Acknowledgment

We thank Fang Xu for her assistance in the synthesis and characterization of single-crystal stishovite crystals. The authors also thank V. Prakapenka and E. Greenberg for their assistance with synchrotron X-ray diffraction experiments at 13ID-D, GSECARS. GSECARS was supported by the National Science Foundation (EAR-0622171) and U.S. Department of Energy (DE-FG0294ER14466) under contract DE-AC0206CH11357. J.F. Lin acknowledges support from Geophysics Program of the U.S. National Science Foundation (EAR-1916941) and the Joint-Use User Program of Institute for Planetary Materials, Okayama University.psu

## References

[1] M. V. Klassen-Neklyudova, *Mechanical twinning of crystals* (Springer Science & Business Media, 2012).
[2] V. K. Wadhawan, Phase Transitions: A Multinational Journal **3**, 3 (1982).
[3] E. K. Salje, Annual Review of Materials Research **42**, 265 (2012).
[4] G. Zhang, F. Liu, T. Gu, Y. Zhao, N. Li, W. Yang, and S. Feng, Advanced Electronic Materials **3**, 1600498 (2017).

[5] M. Guennou, P. Bouvier, G. Garbarino, J. Kreisel, and E. K. Salje, Journal of Physics: Condensed Matter **23**, 485901 (2011).
[6] E. Gregoryanz, R. J. Hemley, H.-k. Mao, and P. Gillet, Physical Review Letters **84**, 3117 (2000).
[7] T. Ishidate and S. Sasaki, Physical review letters **62**, 67 (1989).
[8] M. A. Carpenter, E. K. Salje, and A. Graeme-Barber, European Journal of Mineralogy, 621 (1998).
[9] R. L. Moreira, R. P. Lobo, S. L. Ramos, M. T. Sebastian, F. M. Matinaga, A. Righi, and A. Dias, Physical Review Materials **2**, 054406 (2018).
[10] S. Kaneshima, Physics of the Earth and Planetary Interiors **257**, 105 (2016).
[11] E. K. Salje, Physics reports **215**, 49 (1992).
[12] T. Ishii, H. Kojitani, and M. Akaogi, Journal of Geophysical Research: Solid Earth (2019).
[13] W. Sinclair and A. Ringwood, Nature **272**, 714 (1978).
[14] F. Jiang, G. D. Gwanmesia, T. I. Dyuzheva, and T. S. Duffy, Physics of the Earth and Planetary Interiors **172**, 235 (2009).
[15] J. Haines, J. Leger, and G. Bocquillon, Annual Review of Materials Research **31**, 1 (2001).
[16] D. Andrault, G. Fiquet, F. Guyot, and M. Hanfland, Science **282**, 720 (1998).
[17] K. J. Kingma, R. E. Cohen, R. J. Hemley, and H.-k. Mao, Nature **374**, 243 (1995).
[18] D. Andrault, R. J. Angel, J. L. Mosenfelder, and T. L. Bihan, American Mineralogist **88**, 301 (2003).
[19] R. Hemley, J. Shu, M. Carpenter, J. Hu, H. Mao, and K. Kingma, Solid State Communications **114**, 527 (2000).
[20] M. A. Carpenter, R. J. Hemley, and H. k. Mao, Journal of Geophysical Research: Solid Earth **105**, 10807 (2000).
[21] M. A. Carpenter and E. K. Salje, European Journal of Mineralogy, 693 (1998).
[22] B. Karki, M. Warren, L. Stixrude, G. Ackland, and J. Crain, Physical Review B **55**, 3465 (1997).
[23] R. Yang and Z. Wu, Earth and Planetary Science Letters **404**, 14 (2014).
[24] D. J. Weidner, J. D. Bass, A. Ringwood, and W. Sinclair, Journal of Geophysical Research: Solid Earth **87**, 4740 (1982).
[25] A. Yoneda, T. Cooray, and A. Shatskiy, Physics of the Earth and Planetary Interiors **190**, 80 (2012).
[26] V. Brazhkin, L. McNeil, M. Grimsditch, N. Bendeliani, T. Dyuzheva, and L. Lityagina, Journal of Physics: Condensed Matter **17**, 1869 (2005).
[27] See Supplemental Material at http://XXX for experimental and modelling details as well as complimentary figures and tables. References include [2,14,16,18-26,28-42,48-51].
[28] X. Tong, The University of Texas at Austin, 2014.
[29] J. Yang, X. Tong, J.-F. Lin, T. Okuchi, and N. Tomioka, Scientific reports **5** (2015).
[30] F. Xu, D. Yamazaki, N. Sakamoto, W. Sun, H. Fei, and H. Yurimoto, Earth and Planetary Science Letters **459**, 332 (2017).
[31] S. Fu, J. Yang, N. Tsujino, T. Okuchi, N. Purevjav, and J.-F. Lin, Earth and Planetary Science Letters **518**, 116 (2019).
[32] S. Fu, J. Yang, Y. Zhang, T. Okuchi, C. McCammon, H. I. Kim, S. K. Lee, and J. F. Lin, Geophysical Research Letters (2018).
[33] A. Dewaele, P. Loubeyre, and M. Mezouar, Physical Review B **70**, 094112 (2004).
[34] Y. Fei, A. Ricolleau, M. Frank, K. Mibe, G. Shen, and V. Prakapenka, Proceedings of the National Academy of Sciences **104**, 9182 (2007).
[35] C. Nisr, K. Leinenweber, V. Prakapenka, C. Prescher, S. Tkachev, and S. H. Dan Shim, Journal of Geophysical Research: Solid Earth (2017).
[36] F. Birch, Physical review **71**, 809 (1947).
[37] B. Grocholski, S. H. Shim, and V. Prakapenka, Journal of Geophysical Research: Solid Earth **118**, 4745 (2013).

[38] A. Every, Physical Review B **22**, 1746 (1980).
[39] J.-F. Lin, Z. Mao, J. Yang, and S. Fu, Nature **564**, E18 (2018).
[40] L. Stixrude and C. Lithgow-Bertelloni, Geophysical Journal International **162**, 610 (2005).
[41] M. A. Carpenter, American mineralogist **91**, 229 (2006).
[42] J. Buchen, H. Marquardt, K. Schulze, S. Speziale, T. Boffa Ballaran, N. Nishiyama, and M. Hanfland, Journal of Geophysical Research: Solid Earth **123**, 7347 (2018).
[43] R. Bell and G. Rupprecht, Physical Review **129**, 90 (1963).
[44] M. Born, in *Mathematical Proceedings of the Cambridge Philosophical Society* (Cambridge University Press, 1940), pp. 160.
[45] R. Hazen and J. Mariathasan, Science **216**, 991 (1982).
[46] D. Errandonea and A. B. Garg, Progress in Materials Science **97**, 123 (2018).
[47] G. Benyuan, M. Copic, and H. Cummins, Physical Review B **24**, 4098 (1981).
[48] R. A. Fischer, A. J. Campbell, B. A. Chidester, D. M. Reaman, E. C. Thompson, J. S. Pigott, V. B. Prakapenka, and J. S. Smith, American Mineralogist **103**, 792 (2018).
[49] R. Hill, Proceedings of the Physical Society. Section A **65**, 349 (1952).
[50] J. A. Akins and T. J. Ahrens, Geophysical research letters **29**, 31 (2002).
[51] A. M. Dziewonski and D. L. Anderson, Physics of the earth and planetary interiors **25**, 297 (1981).